A Simple Method for the Design of 1D MEMS Flexural Phononic Crystals

Luca Luschi, Francesco Pieri, and Giuseppe Iannaccone, *Fellow, IEEE*

***Abstract*—We present a simple and computationally inexpensive method to design one-dimensional MEMS flexural phononic crystals with assigned width and central frequency of the acoustic bandgap, based on the analysis of the characteristic polynomial of the acoustic transmission matrix of the crystal elementary cell. Our analysis shows that a high acoustic contrast does not necessarily lead to wide bandgaps, unless the modulation of the mechanical properties is properly chosen. We also demonstrate that the acoustic attenuation inside the bandgap, which is an important design target, is essentially predetermined once that the bandgap width and center have been chosen. The method can be valuable for fast design of phononic crystal devices with applications spanning from sensors to filters and resonators.**

***Index Terms*—Acoustic devices, Acoustic waveguides, Acoustic scattering, Bandstop filters, Micromachining.**

I. Introduction

PHONONIC crystals (PnCs) are structures exhibiting a frequency-selective behavior with respect to the propagation of acoustic waves. Their frequency spectrum is divided into pass bands, where propagation is allowed, alternating with bandgaps, where it is forbidden. The initial interest in PnCs was motivated by the analogy with other waves in periodic lattices: photonic crystals exhibit bandgaps for electromagnetic waves [1], while the periodic potential in crystal lattices produce electron bands in solids. Research in PnCs has evolved in a wide range of subtopics. A general overview on phononic crystals can be found in [2,3].

Several potential applications of PnCs have been envisioned and implemented in various MEMS technologies. The ability to block the propagation of acoustic energy suggested the use of MEMS PnCs to enhance the quality factor of acoustic resonant cavities, created by breaking the periodicity of the crystal [4]. Weinstein and coworkers used acoustic confinement to create an actively sensed CMOS-based resonator, the resonant body transistor [5]. Signal processing blocks such as bandpass filters [6] and demultiplexers [7], have been proposed as well. PnC-based anchors were shown to reduce mechanical losses in standard MEMS resonators [8]. Other applications include mass sensors [9,10], acoustic waveguides [11] and thermal insulators [12].

This work was supported in part by the ENIAC Joint Undertaking under Grant 325622.

The authors are with the Dipartimento di Ingegneria dell'Informazione, Università di Pisa, Pisa, 56122 Italy (e-mail: luca.luschi@for.unipi.it, {f.pieri, g.iannaccone}@iet.unipi.it).

Flexural PnCs, i.e. structures in which flexural (bending) waves are the fundamental mode of propagation, are typically shaped as beams with the direction of propagation along the beam axis. Their properties have been studied in several works [13–15]. An efficient way to model flexural PnCs is the use of transmission matrix models [13,14].

Despite a wide range of theoretical, numerical and experimental investigations, a set of simple practical rules for the design of PnCs, based on the frequency behavior specifications (bandgaps positions and widths, attenuation, etc.), is still lacking. For a series of interesting cases, optimal design has been sought through numerical algorithms. Sigmund and Jensen [16] were the first to use topological optimization in the design of 2D PnCs. They focused on the maximization of the fractional bandgap width, i.e. the ratio of the bandgap width to its central frequency. This approach allows a flexible definition of the target function, but it is computationally very expensive, especially for very fine discretization of the elementary 2D cell. Hussein and coworkers employed genetic algorithms for the design of different classes of PnCs in several works, all based on design targets which are again, essentially, the maximization of the fractional bandgap width. Examples include 1D longitudinal [17], 1D flexural [18], and 2D PnCs [19]. As for the topological optimization, genetic algorithms are computationally very expensive. Furthermore, the mechanical properties (density, elastic moduli) of the material (or materials) involved are not subject to optimization. Olhoff et al [20] implemented an efficient iterative optimization of Euler-Bernoulli flexural beams, aimed at maximizing the distance between two neighboring eigenfrequencies of a finite beam by varying its cross-section with continuity (which is impractical in real devices), without *a priori* assumptions about periodicity. Interestingly, their algorithm led to spatially periodic designs (i.e. finite PnCs) with the unit cell presenting a bandgap between the two eigenfrequencies. As a general limit, all these methods lead to the optimal solution without giving much physical insight about the relative importance of the different design parameters.

In this paper, we present a method for the design of 1D flexural MEMS PnCs, where the periodicity is typically obtained by introducing a regular pattern of holes in the structural layer [4,6,8–10,12]. This choice reduces the degrees of freedom of the design and substantially simplifies the

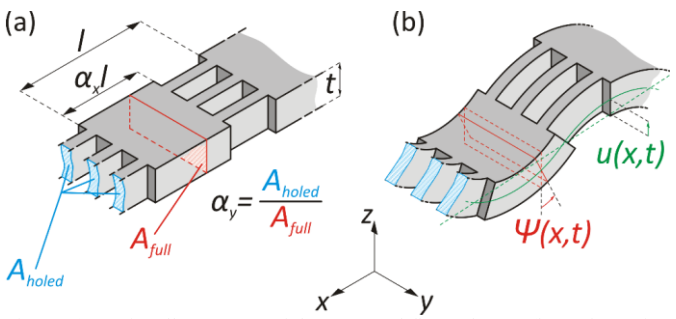

Fig. 1. (a) Unit cell geometry of the proposed flexural PnC. (b) Deformation due to flexural waves.

synthesis. Our method is based on the Euler-Bernoulli (EB) beam theory, and models the acoustic transmission properties of the PnC by using the transmission matrix formalism [13]. We show that, once the bandgap center and width are given, a set of optimal designs can be extracted by following simple rules based on the study of few normalized quantities. We will also show that, contrary to common assumptions, a high acoustic contrast does not necessarily lead to a wide bandgap, and that the attenuation inside the bandgap is essentially predetermined once the bandgap width and center are chosen.

II. Model

The geometry of a typical flexural PnC cell, of length l, is shown in Fig. 1(a). The structural modulation is obtained with rectangular holes, which make the beam properties piecewise-constant functions of x. A PnC is composed by a replica of several cells along the x axis. Each of these cells is composed by a holed segment and a full segment. The flexural wave consists of a deflection along z (Fig. 1(b)). The modulation is defined by two dimensionless parameters: α_x is the length of the full segment normalized to the cell length, and α_y is the area of the holed cross-section normalized to the full cross-section. Both parameters are comprised between 0 and 1. The purpose of the perforations along y is to alter the mechanical properties of the holed segment with respect to the propagation of waves along x. Although these perforations introduce a spatial periodicity also along y, we assume that the flexural deformation is a function of x only (i.e. the PnC is strictly one-dimensional). Additionally, we assume that the holed segment behaves as if constituted of an equivalent material of reduced density and stiffness. The reduction factor is the perforation ratio α_y. The actual number of holes along y in the holed segment does not influence the PnC behavior, as long as it is large enough that the equivalent material hypothesis holds. Having a large number of holes along y increases the surface to volume ratio, a property linked to an increase in sensitivity in resonant mass sensors [10,21–23].

In EB theory, the beam is characterized by two parameters: its bending stiffness *(EI)*, i.e. the product of the Young's modulus E and the moment of inertia of the cross-section I, and the translatory inertia (ρA), i.e. the product of the mass density ρ and the area of the cross-section A.

The state of the beam at any x is described by a state vector $\mathbf{s}(x)$, whose components are the vertical displacement $u(x)$, rotation angle $\psi(x)$, bending moment $m(x)$ and shear force $t(x)$ at the cross-section. To highlight the essential degrees of freedom, we normalize the state vector with respect to l and to the stiffness and inertia of the full segment $(EI)_f$, $(\rho A)_f$, by using the following substitutions:

$$\xi \equiv \frac{x}{l}, \quad U(\xi) \equiv \frac{1}{l}u(\xi l), \quad \Psi(\xi) \equiv \psi(\xi l),$$
$$M(\xi) \equiv \frac{l}{(EI)_f}m(\xi l), \quad T(\xi) \equiv \frac{l^2}{(EI)_f}t(\xi l). \tag{1}$$

With this normalization, the EB beam harmonic equation can be written as:

$$\frac{d}{d\xi}\begin{bmatrix}U(\xi)\\ \Psi(\xi)\\ M(\xi)\\ T(\xi)\end{bmatrix} = \begin{bmatrix}0 & 1 & 0 & 0\\ 0 & 0 & -\frac{(EI)_f}{(EI)} & 0\\ 0 & 0 & 0 & 1\\ -\Omega^2\frac{(\rho A)}{(\rho A)_f} & 0 & 0 & 0\end{bmatrix}\begin{bmatrix}U(\xi)\\ \Psi(\xi)\\ M(\xi)\\ T(\xi)\end{bmatrix} = \mathbf{D}\cdot\mathbf{S}(\xi) \tag{2}$$

where $\mathbf{S}(\xi)$ is the normalized state vector, $\mathbf{D}$ the normalized system matrix, and a normalized angular frequency Ω has been introduced:

$$\Omega \equiv \frac{\omega}{\omega_0}, \quad \omega_0 \equiv \frac{c}{l}, \quad c \equiv \sqrt{\frac{(EI)_f}{l^2(\rho A)_f}} \tag{3}$$

with ω being the angular frequency. The quantity c has the dimensions of a speed, and is defined in accordance with [24]. The normalized system matrix $\mathbf{D}$ is a function of Ω and of the normalized stiffness and inertia only. For our structure the last two quantities are:

$$\frac{(EI)}{(EI)_f} = \frac{(\rho A)}{(\rho A)_f} = \begin{cases}1 & \text{in the full segments}\\ \alpha_y & \text{in the holed segments}\end{cases}. \tag{4}$$

The actual matrix $\mathbf{D}$ depends on the type of segment: we call $\mathbf{D}_f$ the matrix for full segments and $\mathbf{D}_h$ the matrix for holed segments. The transmission matrix of each segment, i.e. the matrix $\mathbf{T}$ such that $\mathbf{S}(\xi+1) = \mathbf{T}\cdot\mathbf{S}(\xi)$, is computed by solving the system (2) for the two types of segments and by combining the solutions. The final expression for $\mathbf{T}$ of a cell is:

$$\mathbf{T} = e^{\alpha_x \mathbf{D}_f} e^{(1-\alpha_x)\mathbf{D}_h} \tag{5}$$

where $e^{\mathbf{M}}$ is the matrix exponential of $\mathbf{M}$. The eigenvalues of $\mathbf{T}$ completely describe the transmission properties of the PnC, and therefore the band structure. Because of the structure of $\mathbf{T}$, the four eigenvalues are determined by only two independent invariants, I_1 and I_2 [25]. In our case, the invariants only depend on α_x, α_y, and Ω. Therefore the expressions of I_1, I_2 are quite simple and can be used to significantly reduce the computational burden. We report them in Appendix A. As I_1, I_2 are not changed by the substitution $\alpha_x \leftrightarrow (1-\alpha_x)$, we limit our analysis to $\alpha_y \in (0,1]$, $\alpha_x \in [0,0.5]$.

The four eigenvalues of $\mathbf{T}$ can be written as $e^{\pm iK_1}$, $e^{\pm iK_2}$, with K_1, K_2 being normalized wavenumbers. Real wavenumbers represent propagating waves, and imaginary (or complex) wavenumbers evanescent waves. The relationship between the wavenumbers and the invariants is [25]:

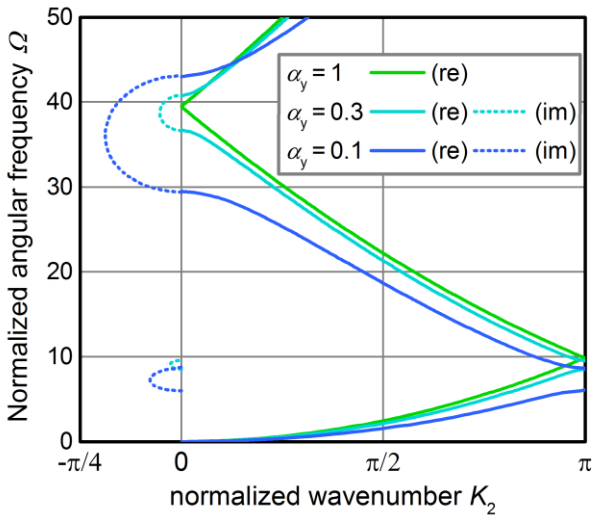

Fig. 2. Typical normalized dispersion relation for a 1D PnC for three different values of α_y. The value of α_x is 0.3 for all the three cases.

$$K_{1,2} = \cos^{-1}\left(\frac{1}{4}\left(-I_1 \pm \sqrt{8 + {I_1}^2 - 4I_2}\right)\right). \qquad (6)$$

The first wavenumber K_1 is always imaginary, whereas K_2 can be complex or real. As K_1 always corresponds to non-propagating solutions, K_2 completely determines the transmission properties of the PnC. From (6), the dispersion relation for the PnC as a function of α_x, α_y can be computed. Typical $K_2(\Omega)$ are shown in Fig. 2. From the design point of view, the most important parameters for a PnC are the location of the stop band (i.e. the frequency limits of the phononic bandgap) and the maximum attenuation within the stopband. For this reason, we proceed to derive the bandgap borders and the attenuation at the bandgap center as a function of the wavenumber K_2.

A frequency is inside a bandgap only if all the wavenumbers have a nonzero imaginary component at that frequency. Therefore, the border of a bandgap is determined by the transition of K_2 from purely real to complex, which takes place when the argument of the arccosine in (6) leaves the interval [-1,+1]. A (normalized) angular frequency Ω is therefore at a bandgap border if and only if the following equation is satisfied:

$$I_2(\alpha_x, \alpha_y, \Omega) \pm 2I_1(\alpha_x, \alpha_y, \Omega) + 2 = 0 \qquad (7)$$

where the minus sign gives the borders of odd order bandgaps, and the plus sign those of even order ones. The bandgap edges can be accurately extracted for any geometry by substituting the corresponding α_x, α_y and numerically solving for the roots of (7), whose only independent variable is Ω. Once that the bandgap edges are known, it is easy to show (see next section) that the attenuation constant at the bandgap center, which essentially corresponds to the frequency of maximum attenuation, can be derived from the imaginary part of K_2 at the bandgap center, which again can be calculated from (6).

III. Design

To design a bandgap in a PnC, we choose as target parameters the center frequency of the gap f_T, and its span Δf around f_T. An important target is also the attenuation per unit length γ within the bandgap, which is the value of the imaginary part of the (denormalized) wavenumber at the center of the bandgap, $\gamma = \left|\mathbf{Im}\left(k_2(f_T)\right)\right|$. As for the design parameters, the geometry of the cell is completely defined by its length l, the perforation ratios α_x and α_y, and possibly the thickness, while the PnC width does not influence the band structure. In the following, we focus on α_x, α_y, and l, as the thickness is commonly constrained by technology in MEMS devices, and cannot be changed as freely as the other dimensions. We limit our analysis to the first three bandgaps, where the EB theory is reasonably accurate.

A useful design specification is the fractional bandwidth $\Delta\Omega_n/\Omega_n$, where Ω_n and $\Delta\Omega_n$ are the normalized bandgap center and width for the first three bandgaps (n = 1,2,3). This ratio is not affected by the normalization and equals $\Delta f/f_T$. In Fig. 3, we present contour plots of this quantity for the first three bandgaps as a function of α_x and α_y. Any point of the contour at the desired $\Delta f/f_T$ value is a valid choice for the design at hand. Synthesis of a PnC for the desired $\Delta f/f_T$ is therefore immediate.

The plots show that, to obtain a high fractional bandwidth, one has to choose a small α_y, i.e. a large acoustic contrast. This is coherent with [16]. With our approach, however, it is also obvious that there are critical ranges of α_x, α_y for which, despite the high contrast, very narrow (or no) bandgaps are obtained. These ranges are very close to the points where the

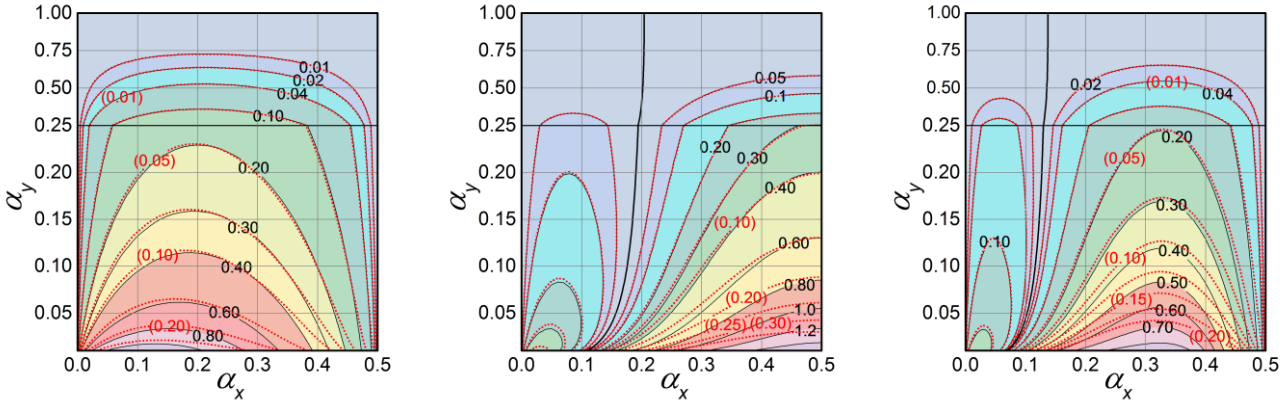

Fig. 3. Normalized bandwidth $\Delta\Omega_n/\Omega_n$ (black solid lines) and normalized attenuation constant Γ_n (red dotted lines) for n = 1, 2, 3 (left to right).

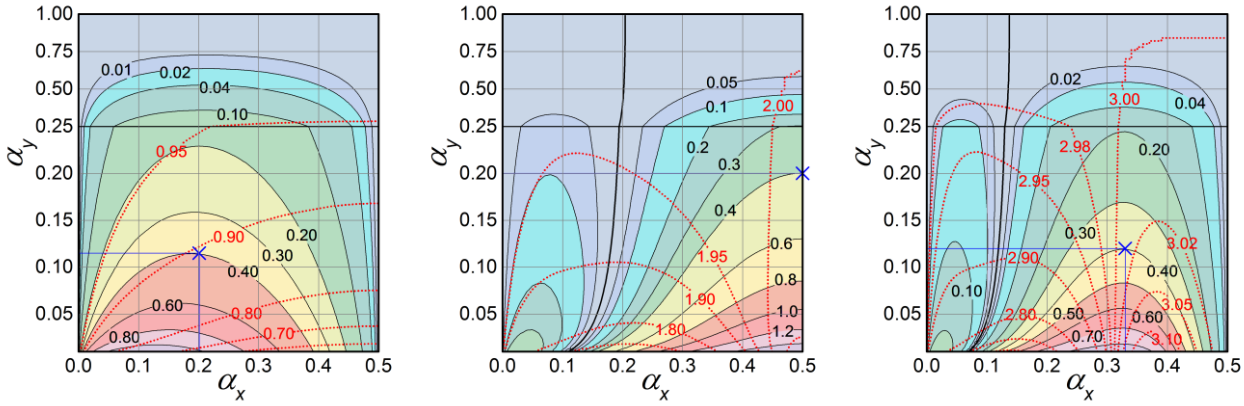

Fig. 4. Normalized bandwidth $\Delta\Omega_n/\Omega_n$ (black solid lines) and length parameter $\sqrt{\Omega_n}/\pi$ (red dotted lines) for n = 1, 2, 3 (left to right). Points for the designs examples in Table 1 are marked with a blue cross.

PnC switches between opposite geometrical phases [26], which are highlighted as thick black lines in Fig. 3. Bandgap closing due to geometrical phase inversion also takes place for α_x= 0.5 for the first and third bandgap.

Points on the same $\Delta f/f_T$ contour line might not correspond to the same attenuation. To investigate the attenuation, we need to define an appropriate figure of merit, based on normalized quantities. We then write the attenuation constant γ as

$$\gamma = \left|\mathbf{Im}\left(k_2(f_T)\right)\right| = \left|\frac{\mathbf{Im}(K_2(\Omega_n))}{l}\right| = \\ = \frac{\left|\mathbf{Im}(K_2(\Omega_n))\right|}{\sqrt{\Omega_n}}\sqrt{2\pi f_T\sqrt{\frac{(\rho A)_f}{(EI)_f}}} = \Gamma_n\sqrt{2\pi f_T\sqrt{\frac{(\rho A)_f}{(EI)_f}}} \qquad (8)$$

where we define $\Gamma_n = \left|\mathbf{Im}\left(K_2(\Omega_n)\right)\right|/\sqrt{\Omega_n}$. The ratio $(\rho A)_f/(EI)_f$ is set by the material and fabrication technology (at constant thickness), and f_T is set by the design target. Γ_n can thus be used as an attenuation FOM, i.e. a quantity that needs to be maximized to maximize the actual attenuation constant γ.

The values of Γ_n are also plotted in Fig. 3. The most striking feature of the plots is that contours for $\Delta\Omega_n/\Omega_n$ and Γ_n are essentially overlapping over most of the design domain, i.e. $\Delta\Omega_n/\Omega_n$ and Γ_n are approximately proportional. For all three bandgaps we have

$$\Gamma_n \approx \frac{1}{4}\frac{\Delta\Omega_n}{\Omega_n}. \qquad (9)$$

This relationship is rigorously true for small deviations from the homogeneous beam, even for beams with non-piecewise constant cross-section (see Appendix B for a proof). The implication of (9) is that every design with prescribed $\Delta f/f_T$ is, from the point of view of the attenuation, substantially equivalent, *regardless of the actual geometry or even of the bandgap order*. A substantial increase in γ (up to few tens of percentage points) can only be obtained in the third bandgap and for very low values of α_y (<0.05), which are very difficult to obtain in a real structure, as they correspond to very narrow structures in the holed segment.

Therefore, once the bandgap limits are chosen, not much can then be done to raise the attenuation in the bandgap. If there is a specification on the minimum total attenuation L_T of the PnC, the total PnC length l_{tot} is roughly fixed by:

$$\exp(\gamma l_{tot}) > L_T \quad \Rightarrow$$
$$l_{tot} > \frac{\ln(L_T)}{\gamma} \approx \frac{4 f_T}{\Delta f}\ln(L_T)\sqrt{\frac{1}{2\pi f_T}\sqrt{\frac{(EI)_f}{(\rho A)_f}}} \qquad (10)$$

where we used (8) and (9). The number of cells is simply the smallest integer larger than l_{tot} divided by the cell length l.

It is also interesting to compare different designs from the point of view of the cell length. We write it as a function of the normalized bandgap center, starting from (3):

$$l = \frac{c}{\omega_0} = \frac{f_T}{\omega_0}\frac{c}{f_T} = \frac{2\pi f_T}{\omega_0}\frac{1}{2\pi f_T}\frac{1}{l}\sqrt{\frac{(EI)_f}{(\rho A)_f}} \quad \Rightarrow$$
$$l = \sqrt{\frac{1}{2\pi f_T}\sqrt{\frac{(EI)_f}{(\rho A)_f}}}\sqrt{\Omega_n} \qquad (11)$$

The cell length for a given design is proportional to $\sqrt{\Omega_n}$. The contour plots of $\sqrt{\Omega_n}/\pi$ for the first, second and third bandgap are superimposed to the ones for $\Delta\Omega_n/\Omega_n$ in Fig. 4. These graphs allow the comparison of different designs from the point of view of the cell length. In addition, through (11), they can be used to calculate the actual cell length. The cell length for a required fractional bandwidth depends both on the specific point chosen on the constant $\Delta\Omega_n/\Omega_n$ curve and on the chosen bandgap order n. As a rule of thumb, the cell length is roughly proportional to n. More precisely, as the n^{th} bandgap opens close to the n^{th} Bragg resonance of the cell, the actual length l for bandgap n is roughly equal to $n/2$ wavelengths of the flexural wave.

How should one choose n, and then $\sqrt{\Omega_n}$ (which is to say l)? The cell length does not affect the total area occupied by the PnC, which is set by (10). However, the smaller is l, the more cells the PnC is composed of. It is desirable to have a large number of cells to ensure that the actual frequency response of a finite PnC matches the one determined by its band structure, which is calculated as if the PnC was infinite. In studying longitudinal crystals of finite length, Hussein [27] concludes that at least 3-4 cells are necessary for the attenuation constant of the PnC to converge to a value close to the one predicted by

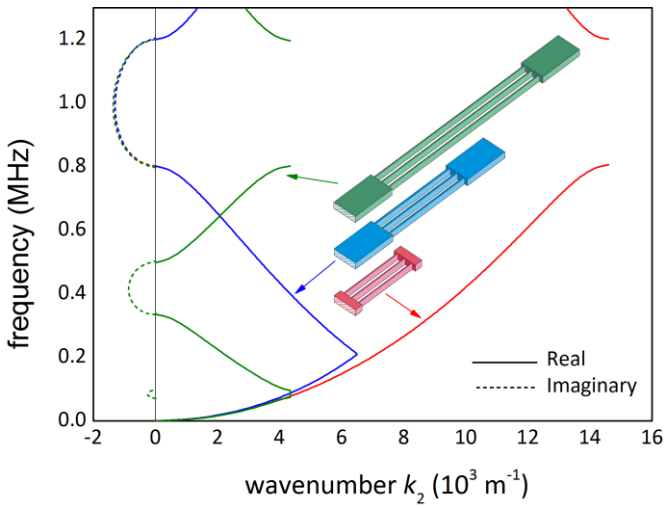

Fig. 5. Band structure of the designed PnCs. The bands for the first, second and third bandgap design are drawn in red, blue and green, respectively. The corresponding elementary cells, with dimensions in scale, are also shown.

the band structure. We then propose the following practical rule: the designer should favor choices of n and $\sqrt{\Omega_n}$ that result in at least 3 cells, and preferably more. This approach seems to rule out the choice of higher order bandgaps (which give a proportionally longer l). Within the limits of our model, however, there might still be a good reason to choose n= 2 or 3 just to ensure that the cell has a large *aspect ratio* (l/t), which is required for the EB equation approximation to hold. Alternatively, a different technology with a smaller thickness can be selected, so that this constraint is relaxed.

A. Design Examples

As an example, we apply our results to the design of a PnC with a bandgap frequency center of f_t = 1 MHz and a width of Δf = 400 kHz. We present and compare three different designs, one for each bandgap order. We set the thickness of the structural layer at 15 µm. The material properties are those of [110] silicon: E = 169 GPa, ρ = 2330 Kg/m^3.

The fractional bandgap width, $\Delta f/f_t$ (and normalized fractional bandwidth $\Delta\Omega_n/\Omega_n$) equals 0.4. This value gives three curves on the contour plots of Fig. 4. Any point laying on these curves is a suitable design point. The points clearly differ significantly for the values of the perforation ratios α_x and α_y. A less marked difference is on the unit cell length, which will be near $n/2$ wavelengths of the flexural wave. This difference can be perceived through the contours of $\sqrt{\Omega_n}/\pi$, shown on the same plots. The choice of the point fixes this quantity and the exact unit cell length through (11), finalizing the design.

Disregarding the effect on cell length, one can simply choose to use the points with the highest α_y, considering that, in practical designs, technological limits of the fabrication process will prevent the fabrication of very small cross-sectional areas in the holed segment, setting a lower limit to α_y. With this choice, the resulting design values are reported in Table 1. These values, along with (6) and (3), can be used to compute the band structures, shown in Fig. 5. For all the three designs, the behavior of the imaginary part of k_2 inside the bandgap is almost identical, confirming the equality of any design in terms of attenuation per unit length. It is worth noticing that, in the design with the second bandgap (blue lines) the first bandgap is closed since the value of α_x= 0.5 matches the condition for the geometric phase inversion effect on the first gap.

TABLE I
PARAMETERS FOR THE THREE DESIGN EXAMPLES

Bandgap number	l (µm)	α_x (/)	α_y (/)
1	215.3	0.2	0.115
2	482.4	0.5	0.2
3	724.6	0.33	0.12

IV. CONCLUSIONS

We have presented a systematic approach for the design of one-dimensional flexural PnCs fabricated by regular perforations. Given the desired band gap center and width, the whole design can be finalized by means of the normalized plots of the fractional band gap width $\Delta\Omega_n/\Omega_n$ and of the square root of the band gap center $\sqrt{\Omega_n}/\pi$ for the different band gap orders n. Differently from many proposed methods, where only the optimal design is given, here a complete mapping of all the meaningful quantities over the whole design space is known *a priori,* so that the effect of changes in the design can be evaluated very quickly. Moreover, the normalization reduces the number of design variables and makes the method independent of the materials properties. Remarkably, the attenuation per unit length is strongly constrained to the design targets, so that the choice among different design points is only ruled by geometrical considerations such as the maximum obtainable acoustic contrast, the total number of cells along the finite PnC and the aspect ratio of the cell itself. We demonstrated that this constraint is a general property of flexural PnCs. Experimental validation on piezoelectrically actuated, crystalline silicon devices is planned.

APPENDIX A

The two independent invariants for the matrix **T** are:

$$I_1(\alpha_x,\alpha_y,\Omega) = \frac{1}{2\alpha_y}\big((1-\alpha_y)^2\cos(\sqrt{\Omega}\alpha_x)\cosh(\sqrt{\Omega}(1-\alpha_x)) + (1-\alpha_y)^2\cos((1-\alpha_x)\sqrt{\Omega})\cosh(\alpha_x\sqrt{\Omega}) - (1+\alpha_y)^2\cos(\sqrt{\Omega}) - (1+\alpha_y)^2\cosh(\sqrt{\Omega})\big) \quad (12)$$

$$I_2(\alpha_x,\alpha_y,\Omega) = \frac{1}{16\alpha_y^2}\big(2\cos((\alpha_x-1)\sqrt{\Omega})\cosh((\alpha_x-1)\sqrt{\Omega})\big((\alpha_y-1)^4\cos(\alpha_x\sqrt{\Omega})\cosh(\alpha_x\sqrt{\Omega}) - 2(\alpha_y^2-1)^2\big) + \alpha_y\big((\alpha_y-2)\big((\alpha_y-2)\alpha_y+2\big)\big(2\sin((\alpha_x-1)\sqrt{\Omega})\sin(\alpha_x\sqrt{\Omega})\sinh((\alpha_x-1)\sqrt{\Omega})\sinh(\alpha_x\sqrt{\Omega}) + \cos((2\alpha_x-1)\sqrt{\Omega})\cosh((2\alpha_x-1)\sqrt{\Omega})\big) - 4\alpha_y\big(\alpha_y^2-2\big)\cos(\alpha_x\sqrt{\Omega})\cosh(\alpha_x\sqrt{\Omega})\big) + 2\sin((\alpha_x-1)\sqrt{\Omega})\sin(\alpha_x\sqrt{\Omega})\sinh((\alpha_x-1)\sqrt{\Omega})\sinh(\alpha_x\sqrt{\Omega}) - 4\cos(\alpha_x\sqrt{\Omega})\cosh(\alpha_x\sqrt{\Omega}) + \cos((2\alpha_x-1)\sqrt{\Omega})\cosh((2\alpha_x-1)\sqrt{\Omega}) + 4\alpha_y^4 + 24\alpha_y^2 + (\alpha_y(\alpha_y+6)+1)^2\cos(\sqrt{\Omega})\cosh(\sqrt{\Omega}) + 4\big). \quad (13)$$

APPENDIX B

The approximation in (9) is exact for a generic phononic crystal with the hypothesis that its properties differ only slightly from those of a homogenous beam (a beam with uniform cross-section and material properties). We therefore analyze the effect of a small perturbation over the normalized dispersion relation $K_2(\Omega)$ of a homogeneous beam. Preliminarily, we observe that, in a homogeneous flexural beam, the dispersion relation is simply

$$K_2 = \pm\sqrt{\Omega}. \tag{14}$$

Without loss of generality, we assume that a periodicity is introduced in a homogeneous beam by changing a perturbation parameter $\delta\alpha$, and that the case $\delta\alpha = 0$ corresponds to the homogenous case. A change in α can be related to a change in geometry, density, stiffness, or their combination. Because of the symplecticity of the transmission matrix (which corresponds to the fact that the dispersion relation is invariant by sign reversal), the characteristic polynomial of **T** can be written as [25]:

$$\lambda^4 + I_1(\delta\alpha,\Omega)\lambda^3 + I_2(\delta\alpha,\Omega)\lambda^2 + I_1(\delta\alpha,\Omega)\lambda + 1 = 0 \tag{15}$$

which can be further factorized into:

$$(\lambda^2 + I_E(\delta\alpha,\Omega)\lambda + 1)(\lambda^2 + I_P(\delta\alpha,\Omega)\lambda + 1) = 0. \tag{16}$$

Simple relationships exist between I_1, I_2 and I_E, I_P. The first factor in (16) corresponds to the eigenvalues $e^{\pm iK_1}$ (which always give rise to evanescent waves), and the second to the eigenvalues $e^{\pm iK_2}$. The information on the dispersion relation is thus contained in $I_P(\delta\alpha,\Omega)$ only. Solving for the roots of the second factor in (16), the generic dispersion relation is obtained:

$$K_2 = \pm i \ln\left(\frac{1}{2}\left(-I_P + \sqrt{{I_P}^2 - 4}\right)\right) + 2\pi p, \quad p \in \mathbb{Z}. \tag{17}$$

In a homogenous beam, (17) reduces to (14). The condition for K_2 to be real, i.e. for Ω to be **outside** of a bandgap is:

$$-2 \le I_P(\delta\alpha,\Omega) \le 2 \tag{18}$$

It is possible to show that $I_P > 2$ corresponds to the opening of odd order bandgaps, and $I_P < -2$ to even order bandgaps. For brevity, we concentrate on the former case (derivation is identical for the latter). In a homogenous beam, (18) is always verified, but I_P assumes the value 2 for a numerable set of values Ω_{n0} of the frequency. A perturbation of the homogeneity (i.e. a change in $\delta\alpha$) opens a bandgap around any of these frequencies. To study this effect, we define:

$$\delta I_P(\delta\alpha,\delta\Omega) = I_P(\delta\alpha,\Omega_{n0}+\delta\Omega) - 2. \tag{19}$$

Inside the opening bandgap, δI_P is always positive. For small perturbations and odd bandgaps, (17) can be approximated as:

$$K_2 \approx n\pi \pm i\sqrt{\delta I_P(\delta\alpha,\delta\Omega)}, \quad n \text{ odd}. \tag{20}$$

It is immediate that in the homogeneous case no bandgap opens, and thus $\delta I_P(0,\delta\Omega) \le 0$. Furthermore, as a change in $\delta\alpha$ opens the bandgap, $\delta I_P(\delta\alpha,0) \ge 0$. The point (0,0) is then a saddle point for $\delta I_P(\delta\alpha,\delta\Omega)$. We can now write the second order series expansion of δI_P around the point (0,0):

$$\delta I_P(\delta\alpha,\delta\Omega) \approx \frac{1}{2}I_{P,\alpha\alpha}\,\delta\alpha^2 + I_{P,\alpha\Omega}\,\delta\alpha\delta\Omega + \frac{1}{2}I_{P,\Omega\Omega}\,\delta\Omega^2 \tag{21}$$

where we used comma notation for partial derivatives, and exploited the fact that, because of the existence of the saddle point, first order derivatives are zero. Substituting (21) in (20):

$$K_2 \approx n\pi \pm i\sqrt{\frac{1}{2}I_{P,\alpha\alpha}\,\delta\alpha^2 + I_{P,\alpha\Omega}\,\delta\alpha\delta\Omega + \frac{1}{2}I_{P,\Omega\Omega}\,\delta\Omega^2}, \quad n \text{ odd}. \tag{22}$$

Equation (22) is then an approximate expression for the dispersion relation in the vicinity of the opening bandgap, from which we can determine the normalized bandgap width $\Delta\Omega_n$, its center Ω_n, and normalized attenuation Γ_n. Straightforward calculations give:

$${\Delta\Omega_n}^2 = 4\frac{{I_{P,\alpha\Omega}}^2 - I_{P,\alpha\alpha}I_{P,\Omega\Omega}}{{I_{P,\Omega\Omega}}^2}\delta\alpha^2 \tag{23}$$

$$\Omega_n = \Omega_{n0} - \frac{I_{P,\alpha\Omega}}{I_{P,\Omega\Omega}}\delta\alpha \approx \Omega_{n0} \tag{24}$$

$${\Gamma_n}^2 = \frac{|Im(K_2(\Omega_n))|^2}{\Omega_n} = \frac{{I_{P,\alpha\Omega}}^2 - I_{P,\alpha\alpha}I_{P,\Omega\Omega}}{2|I_{P,\Omega\Omega}|\Omega_{n0}}\delta\alpha^2. \tag{25}$$

The ratio between Γ_n and the fractional bandwidth can thus be written as:

$$\left(\frac{\Gamma_n}{\frac{\Delta\Omega_n}{\Omega_n}}\right)^2 = \frac{1}{8}\Omega_{n0}\left|I_{P,\Omega\Omega}\right|. \tag{26}$$

The values of Ω_{n0} and $I_{P,\Omega\Omega}$ can be determined by equating (14) and (22) in the homogeneous ($\delta\alpha = 0$) case:

$$K_2(0,\delta\Omega) = \pm\sqrt{\Omega_{n0}+\delta\Omega} \approx \pm\sqrt{\Omega_{n0}} \pm \frac{1}{2\sqrt{\Omega_{n0}}}\delta\Omega = \\ = n\pi \pm i\sqrt{(I_{P,\Omega\Omega}/2)\,\delta\Omega^2}. \tag{27}$$

The left and right rides of (27) are now two approximations of the same dispersion relation. Comparison of the two gives:

$$\Omega_{n0} = (n\pi)^2, \quad I_{P,\Omega\Omega} = -\frac{1}{2\Omega_{n0}} = -\frac{1}{2(n\pi)^2}. \tag{28}$$

Finally, substitution of (28) in (26) gives:

$$\Gamma_n = \frac{1}{4}\frac{\Delta\Omega_n}{\Omega_n}. \tag{29}$$

REFERENCES

[1] J.D. Joannopoulos, S.G. Johnson, J.N. Winn, R.D. Meade, Photonic Crystals: Molding the Flow of Light (Second Edition), 2011. https://books.google.com/books?hl=it&lr=&id=owhE36qiTP8C&pgis=1 (accessed February 17, 2016).

[2] M.I. Hussein, M.J. Leamy, M. Ruzzene, Dynamics of Phononic Materials and Structures: Historical Origins, Recent Progress, and Future Outlook, Appl. Mech. Rev. 66 (2014) 040802. doi:10.1115/1.4026911.

[3] R.H. Olsson III, I. El-Kady, Microfabricated phononic crystal devices and applications, Meas. Sci. Technol. 20 (2009) 012002. doi:10.1088/0957-0233/20/1/012002.

[4] S. Mohammadi, A. Adibi, Waveguide-Based Phononic Crystal Micro/Nanomechanical High-Q Resonators, J. Microelectromechanical Syst. 21 (2012) 379–384. doi:10.1109/JMEMS.2011.2174426.

[5] B. Bahr, R. Marathe, D. Weinstein, Theory and Design of Phononic Crystals for Unreleased CMOS-MEMS Resonant Body Transistors, J. Microelectromechanical Syst. 24 (2015) 1520–1533. doi:10.1109/JMEMS.2015.2418789.

[6] S. Mohammadi, A. Khelif, A. Adibi, VHF phononic band gap band

pass filters using coupled resonator acoustic waveguides (CRAW), IEEE Int. Ultrason. Symp. IUS. (2011) 989–991. doi:10.1109/ULTSYM.2011.0242.

[7] S. Mohammadi, A. Adibi, On chip complex signal processing devices using coupled phononic crystal slab resonators and waveguides, AIP Adv. 1 (2011) 0–7. doi:10.1063/1.3676168.

[8] L. Sorenson, J.L. Fu, F. Ayazi, One-dimensional linear acoustic bandgap structures for performance enhancement of AlN-on-Silicon micromechanical resonators, in: 2011 16th Int. Solid-State Sensors, Actuators Microsystems Conf., IEEE, 2011: pp. 918–921. doi:10.1109/TRANSDUCERS.2011.5969685.

[9] P. Li, F. Li, Y. Liu, F. Shu, J. Wu, Y. Wu, Temperature insensitive mass sensing of mode selected phononic crystal cavity, J. Micromechanics Microengineering. 25 (2015) 125027. doi:10.1088/0960-1317/25/12/125027.

[10] L. Luschi, F. Pieri, Design of MEMS mass sensors based of flexural phononic crystals, in: 2015 XVIII AISEM Annu. Conf., 2015: pp. 1–4. doi:10.1109/AISEM.2015.7066802.

[11] D. Hatanaka, I. Mahboob, K. Onomitsu, H. Yamaguchi, Phonon waveguides for electromechanical circuits., Nat. Nanotechnol. 9 (2014) 520–4. doi:10.1038/nnano.2014.107.

[12] P.E. Hopkins, C.M. Reinke, M.F. Su, R.H. Olsson, E.A. Shaner, Z.C. Leseman, et al., Reduction in the thermal conductivity of single crystalline silicon by phononic crystal patterning, Nano Lett. 11 (2011) 107–112. doi:10.1021/nl102918q.

[13] L. Liu, M.I. Hussein, Wave Motion in Periodic Flexural Beams and Characterization of the Transition Between Bragg Scattering and Local Resonance, J. Appl. Mech. 79 (2012) 011003. doi:10.1115/1.4004592.

[14] G. Carta, M. Brun, Bloch-Floquet waves in flexural systems with continuous and discrete elements, Mech. Mater. 87 (2015) 11–26. doi:10.1016/j.mechmat.2015.03.004.

[15] L. Junyi, D.S. Balint, An inverse method to determine the dispersion curves of periodic structures based on wave superposition, J. Sound Vib. 350 (2015) 41–72. doi:10.1016/j.jsv.2015.03.041.

[16] O. Sigmund, J. Sondergaard Jensen, Systematic design of phononic band-gap materials and structures by topology optimization, Philos. Trans. R. Soc. A Math. Phys. Eng. Sci. 361 (2003) 1001–1019. doi:10.1098/rsta.2003.1177.

[17] M.I. Hussein, K. Hamza, G.M. Hulbert, R. a. Scott, K. Saitou, Multiobjective evolutionary optimization of periodic layered materials for desired wave dispersion characteristics, Struct. Multidiscip. Optim. 31 (2006) 60–75. doi:10.1007/s00158-005-0555-8.

[18] O. Bilal, M. El-Beltagy, M. Hussein, Optimal Design of Periodic Timoshenko Beams using Genetic Algorithms, in: 52nd AIAA/ASME/ASCE/AHS/ASC Struct. Struct. Dyn. Mater. Conf., American Institute of Aeronautics and Astronautics, Reston, Virigina, 2011. doi:10.2514/6.2011-1898.

[19] O.R. Bilal, M.I. Hussein, Ultrawide phononic band gap for combined in-plane and out-of-plane waves, Phys. Rev. E. 84 (2011) 065701. doi:10.1103/PhysRevE.84.065701.

[20] N. Olhoff, B. Niu, G. Cheng, Optimum design of band-gap beam structures, Int. J. Solids Struct. 49 (2012) 3158–3169. doi:10.1016/j.ijsolstr.2012.06.014.

[21] S. Lenci, F. Pieri, L. Haspeslagh, J. De Coster, S. Decoutere, A. Maestre Caro, et al., Stiction-free poly-SiGe resonators for monolithic integration of biosensors with CMOS, in: 2011 16th Int. Solid-State Sensors, Actuators Microsystems Conf., IEEE, 2011: pp. 2136–2139. doi:10.1109/TRANSDUCERS.2011.5969323.

[22] L. Luschi, F. Pieri, An analytical model for the resonance frequency of square perforated Lamé-mode resonators, Sensors Actuators B Chem. 222 (2016) 1233–1239. doi:10.1016/j.snb.2015.07.085.

[23] L. Luschi, F. Pieri, An analytical model for the determination of resonance frequencies of perforated beams, J. Micromechanics Microengineering. 24 (2014) 055004. doi:10.1088/0960-1317/24/5/055004.

[24] L. Liu, M.I. Hussein, Wave Motion in Periodic Flexural Beams and Characterization of the Transition Between Bragg Scattering and Local Resonance, J. Appl. Mech. 79 (2012) 011003. doi:10.1115/1.4004592.

[25] F. Romeo, a Luongo, Invariant representation of propagation properties for bi-coupled periodic structure, J. Sound Vib. 257 (2002) 869–886. doi:10.1006/jsvi.5065.

[26] M. Xiao, G. Ma, Z. Yang, P. Sheng, Z.Q. Zhang, C.T. Chan, Geometric phase and band inversion in periodic acoustic systems, Nat. Phys. 11 (2015) 240–244. doi:10.1038/nphys3228.

[27] M.I. Hussein, G.M. Hulbert, R.A. Scott, Dispersive elastodynamics of 1D banded materials and structures: analysis, J. Sound Vib. 289 (2006) 779–806. doi:10.1016/j.jsv.2005.02.030.